1

On the Use of Airborne Imaging Spectroscopy Data for the Automatic Detection and Delineation of Surface Water Bodies

Mathias Bochow[1,2] et al.[*]
[1]*Helmholtz Centre Potsdam – GFZ German Research Centre for Geosciences*
[2]*Alfred Wegener Institute for Polar and Marine Research in the Helmholtz Association*
Germany

1. Introduction

There is economical and ecological relevance for remote sensing applications of inland and coastal waters: The European Union Water Framework Directive (European Parliament and the Council of the European Union, 2000) for inland and coastal waters requires the EU member states to take actions in order to reach a good ecological status in inland and coastal waters by 2015. This involves characterization of the specific trophic state and the implementation of monitoring systems to verify the ecological status. Financial resources at the national and local level are insufficient to assess the water quality using conventional methods of regularly field and laboratory work only. While remote sensing cannot replace the assessment of all aquatic parameters in the field, it powerfully complements existing sampling programs and offers the base to extrapolate the sampled parameter information in time and in space.

The delineation of surface water bodies is a prerequisite for any further remote sensing based analysis and even can by itself provide up-to-date information for water resource management, monitoring and modelling (Manavalan *et al.*, 1993). It is further important in the monitoring of seasonally changing water reservoirs (e.g., Alesheikh *et al.*, 2007) and of short-term events like floods (Overton, 2005). Usually the detection and delineation of surface water bodies in optical remote sensing data is described as being an easy task. Since water absorbs most of the irradiation in the near-infrared (NIR) part of the electromagnetic spectrum water bodies appear very dark in NIR spectral bands and can be mapped by simply applying a maximum threshold on one of these bands (Swain & Davis, 1978: section 5-4). Many studies took advantage of this spectral behaviour of water and applied methods like single band density slicing (e.g., Work & Gilmer, 1976), spectral indices (McFeeters, 1996, Xu, 2006) or multispectral supervised classification (e.g., Frazier & Page, 2000, Lira, 2006). However, all of

[*] Birgit Heim[2], Theres Küster[1], Christian Rogaß[1], Inka Bartsch[2], Karl Segl[1], Sandra Reigber[3,4] and Hermann Kaufmann[1]
[1]*Helmholtz Centre Potsdam – GFZ German Research Centre for Geosciences, Germany*
[2]*Alfred Wegener Institute for Polar and Marine Research in the Helmholtz Association, Germany*
[3]*RapidEye AG, Germany*
[4]*Technical University of Berlin, Germany*

these methods have the drawback that they are not fully automated since the analyst has to select a scene-specific threshold (Ji *et al.*, 2009) or training pixels. Moreover there are certain situations where these methods lead to misclassification. For instance, water constituents in turbid water as well as water bottom reflectance and sun glint can raise the reflectance spectrum of surface water even in the NIR spectral range up to a reflectance level which is typical for dark surfaces on land such as dark rocks (e.g., basalt, lava), bituminous roofing materials and in particular shadow regions. Consequently, Carleer & Wolff (2006) amongst others found the land cover classes water and shadow to be highly confused in image classifications. This problem especially occurs in environments where both, a high amount of shadow and water regions can exist, such as urban landscapes, mountainous landscapes or cliffy coasts as well as generally in images with water bodies and cloud shadows.

In this investigation we focus on the development of a new surface water body detection algorithm that can be automatically applied without user knowledge and supplementary data on any hyperspectral image of the visible and near-infrared (VNIR) spectral range. The analysis is strictly focused on the VNIR part of the electromagnetic spectrum due to the growing number of VNIR imaging spectrometers. The developed approach consists of two main steps, the selection of potential water pixels (section 4.1) and the removal of false positives from this mask (sections 4.2 and 4.3). In this context the separation between water bodies and shadowed surfaces is the most challenging task which is implemented by consecutive spectral and spatial processing steps (sections 4.3.1 and 4.3.2) resulting in very high detection accuracies.

2. Optical fundamentals of water remote sensing

For the spectral identification of water pixels and the separation from other dark surfaces and shadows it is necessary to understand the influencing factors contributing to the surface reflectance of water bodies and especially to the optical complexity and variability of coastal and inland waters. The spectral reflectance of water (its apparent water colour) is a function of the optically visible water constituents (suspended and dissolved) and the depth of the water body (Effler & Auer, 1987, Bukata *et al.*, 1991, Bukata *et al.*, 1995). The concentration and composition of (i) phytoplankton, (ii) suspended particulate matter (SPM) and (iii) dissolved organic matter loading dominate the optical properties of natural waters. Shallow coastal and inland waters may also contain the spectral signal contribution from the bottom reflectance that significantly differs with the various materials (mainly sands (different colours), muds (different colours), macrophytes (different abundances, groups and compositions), reefs (different structures, different colours).

Smith & Baker (1983) and Pope & Fry (1997) provide absorption spectra of pure water derived from laboratory investigations. The Ocean Optic Protocols (Müller & Fargion, 2002) propose the absorption spectra of Sogandares & Fry (1997) for wavelengths between 340 nm and 380 nm, Pope & Fry (1997) for wavelengths between 380 nm and 700 nm, and Smith & Baker (1983) for wavelengths between 700 nm and 800 nm. Buiteveld et al. (1994) investigated the temperature dependant water absorption properties. Morel (1974) provides spectral values of the pure water volume scattering coefficient at specific temperatures and salinity, and the directional phase function. Gege (2005) used the data from the afore listed publications to construct the WASI absorption spectrum of pure water. This absorption spectrum formed the basis of the knowledge-based algorithm for water identification presented in Section 4.3.1.

Specular reflection of direct sunlight at the water surface into the sensor should be avoided by choosing a different viewing geometry. Specular reflection of the diffuse incoming sky radiation at the water surface can not be avoided and accounts up to 2 to 4 % of the overall surface reflectance that is measured by a sensor. Thus, most of the incoming radiation penetrates the water. Wavelengths larger than 800 nm are entirely absorbed by a large water column of pure water, so reflectance and transmission are no more significant in those longer wavelengths. As solar and sky radiation transmits into the water, the scattering by suspended particles and the absorption by suspended and dissolved water constituents are the water colouring processes. The wavelength peak of the spectral reflectance from transparent waters lies in the blue wavelength range and in this case energy may be reflected from the bottom up of up to 20 meters deep. If waters are less transparent due to higher concentrations of phytoplankton and sediments, and if the back-reflected signal from the bottom in shallow water bodies reach back to the air/water interface, there is significant reflectance from the water body also at the longer wavelength ranges (green to red) and there is a rise of the water-leaving reflectance even in the NIR wavelength region. In the case of phytoplankton blooming, high sediment loads or shallow waters with a bright bottom reflectance the water leaving signal significantly rises in the NIR and the overall reflectance may reach near 10 to 15 %. Therefore, there is no mono-type of the shape and the magnitude of the spectral water-leaving reflectance (Fig. 1). Inland and coastal waters may exhibit bright, turbid waters due to phytoplankton and sediments or bottom reflectance of their shallow areas, and in these cases simple thresholding techniques are no solution for the extraction and delineation of water bodies.

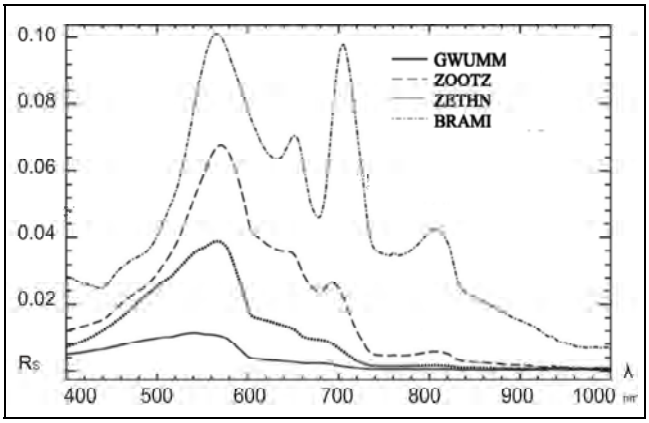

Fig. 1. Surface reflectance spectra, R_S (scale 0-1), of different inland waters (Rheinsberg Lake District, Germany) representing different water colours (Reigber, in prep). GWUMM, Grosser Wummsee, highly transparent, oligotrophic (nature reserve, densely forested); ZOOTZ, Zootzensee, mesotroph (rural, forested); ZETHN, Zethner See, turbid, mesotroph-eutrophic (rural); BRAMI, Braminsee, highly turbid, polytrophic (fish farming, rural)

3. Overview of existing methods for water body mapping

In the majority of algorithms for water body mapping a spectral band in the NIR spectral region plays an important role due to the high absorption of water and resulting high

contrast in NIR bands to many other surface types. However, Manavalan et al. (1993) found that optimal cut-of gray values for individual spectral bands have to be carefully adjusted and are varying between different images. Band ratios or spectral indices are often used to mitigate spectral differences between images and also to enhance the contrast between surface types. Consequently, indices like the NDWI (McFeeters, 1996) (Equation 1) and MNDWI (Xu, 2006) (Equation 2) have been developed. Basically, the authors suggest a default threshold value of zero for these indices, i.e. gray values greater than zero represent water pixels. However, the comparative study of Ji et al. (2009) showed that an image and landscape specific adjustment of threshold values can improve results. Therefore, these methods are not fully suitable for automation. Further, NDWI shows high false positives in build-up areas (Xu, 2006). Xu developed the MNDWI to enhance the separation between water and built-up areas using Landsat ETM+ images. However, in high spatial resolution images there is no single spectral profile for the class "built-up areas" (Roessner *et al.*, 2011) and many man-made materials have positive NDWI and/or MNDWI values (Fig. 2 and Tab. 1). This is also true for shadow over non-vegetated areas. Fig. 3 shows that indices like the NDWI are not suitable for water body mapping in urban areas using high spatial resolution images since no threshold value can be found for which both, false positives and false negatives are low.

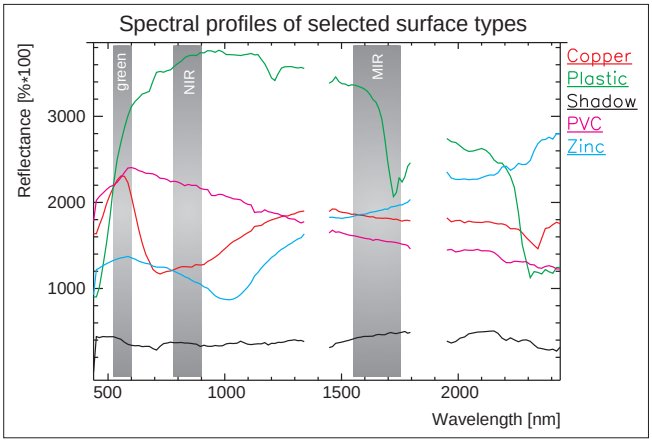

Fig. 2. Reflectance spectra of man-made materials with positive NDWI and/or MNDWI values. The gray bars indicate Landsat TM bands which are typically taken for calculating the NDWI and MNDWI. The spectra were collected from the test site Potsdam

Surface type	**NDWI**	**MNDWI**
Copper	0.28	0.10
Plastic	-0.13	0.01
Shadow	0.03	-0.10
PVC	0.03	0.20
Zinc	0.09	-0.17

Table 1. Corresponding index values of the spectra in Fig. 2

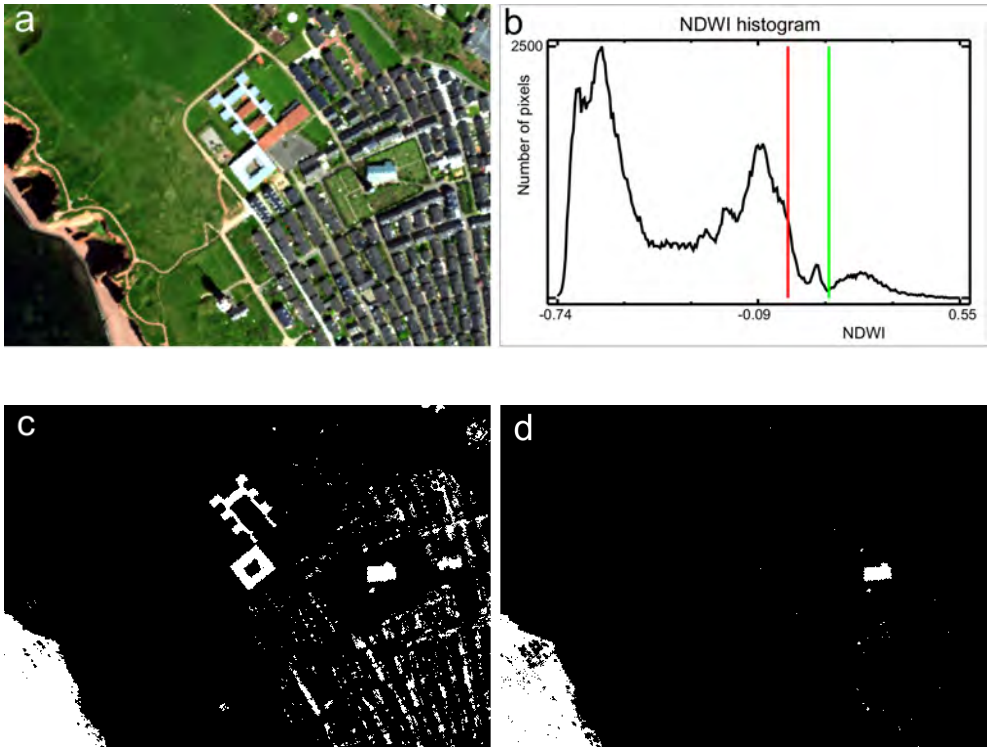

Fig. 3. True colour composite of an AISA image of Helgoland, Germany, with (b) histogram of the NDWI, (c) Water mask by threshold 0 (red line in histogram) on the NDWI; (d) Water mask by threshold 0.13 (green line in histogram) on the NDWI. In image c the water body (bottom left side) is almost totally included in the water mask but many urban features are so, too. In image d some parts of the water body are already lost but still some urban features are present

$$NDWI = \frac{(green - NIR)}{(green + NIR)} \tag{1}$$

where *green* is a green band and *NIR* is a NIR band

$$MNDWI = \frac{(green - MIR)}{(green + MIR)} \tag{2}$$

where *green* is a green band and *MIR* is a middle infrared band

In addition to the spectral-based approaches object-oriented methods have been developed for water body mapping (e.g. Xiao & Tien, 2010). However, since these methods use size and shape features they have to be adjusted individually for each application and can not be used for mapping ponds, rivers and coastal waters with the same configuration at the same time.

4. Material and methods

In this investigation a knowledge-based algorithm for the automated mapping of water bodies was developed based on a spectral database from five airborne hyperspectral datasets from the two German cities Berlin (two datasets) and Potsdam, and the German island Helgoland (two datasets) (Tab. 2). Five independent datasets were used for validation (Tab. 2). The selected scenes comprise urban, rural and coastal landscapes as well as different sensors to prove the wide applicability of the developed approach. The AISA Eagle sensor is an airborne VNIR pushbroom scanner (400 – 970 nm) with 12 bit radiometric resolution and variable spatial and spectral binning options, the latter resulting in mean spectral sampling intervals between 1.25 nm and 9.2 nm (Spectral Imaging Ltd., 2011) and

Test site	Sensor	Acquisition date, time (UTC)	Pixel size (rounded)
Berlin (*urban*)	HyMap	20.06.2005, 09:38 * 20.06.2005, 10:12 *	4 m 4 m
Potsdam (*urban*)	HyMap	07.07.2004, 10:29 *	4 m
Helgoland (*coastal*)	AISA Eagle	09.05.2008, 08:32 * 09.05.2008, 09:26 ° 09.05.2008, 09:41 *	1 m 1 m 1 m
Rheinsberg (rural)	HyMap	20.06.1999, 10:46 °	10 m
Dresden (*urban*)	HyMap	07.07.2004, 09:39 °	4 m
Mönchsgut (*coastal*)	HyMap	03.09.1998, 13:47 °	6 m
Döberitzer Heide (*rural*)	AISA Eagle	19.08.2009, 11:42 °	2 m

* Datasets analyzed during algorithm development
° Independent datasets for validation

Table 2. Dataset-specific characteristics

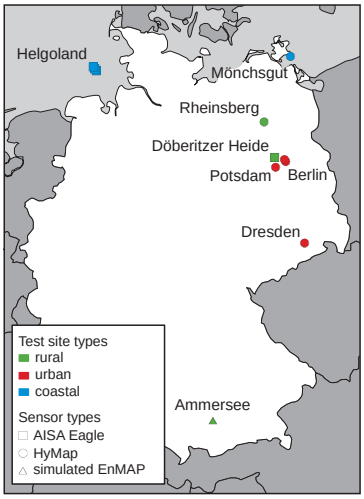

Fig. 4. Location of the test sites within Germany

488 to 60 spectral bands, respectively. The mean spectral sampling interval of the analyzed datasets is 2.3 nm for "Döberitzer Heide" and 4.6 nm for "Helgoland". The HyMap sensor is an airborne VNIR-SWIR whiskbroom scanner with 16 bit radiometric resolution consisting of four detector modules with mean spectral sampling intervals of 15 nm (VIS and NIR), 13 nm (SWIR1) and 17 nm (SWIR2) (Cocks *et al.*, 1998). The 128 spectral bands cover the spectral region from 440 nm to 2500 nm.

Water detection is a trivial task as long as there are no other dark surfaces present in the image. Unfortunately, the most prominent spectral characteristic of water pixels – water pixels are very dark – also applies to a couple of other surfaces such as dark rocks (e.g., lava, basalt) or bituminous roofing materials and especially to pixels covered by shadow. To account for this, we developed a two-step approach that firstly masks low albedo pixels as potential water pixels (section 4.1) and secondly applies a process of elimination to consecutively remove false positives (sections 4.2 and 4.3).

4.1 Masking potential water pixels

Masking of potential water pixels is done by thresholding a spectral mean image of all NIR bands between 860 nm and 900 nm of a sensor. As pointed out before water absorbs most of the incident energy in the NIR spectral region exhibiting a high brightness contrast to the majority of other surfaces. However, since every scene is different a scene-specific threshold has to be found. This is done automatically based on the histogram of the NIR spectral mean image (Fig. 5). After finding the histogram peak of low albedo surfaces (first local

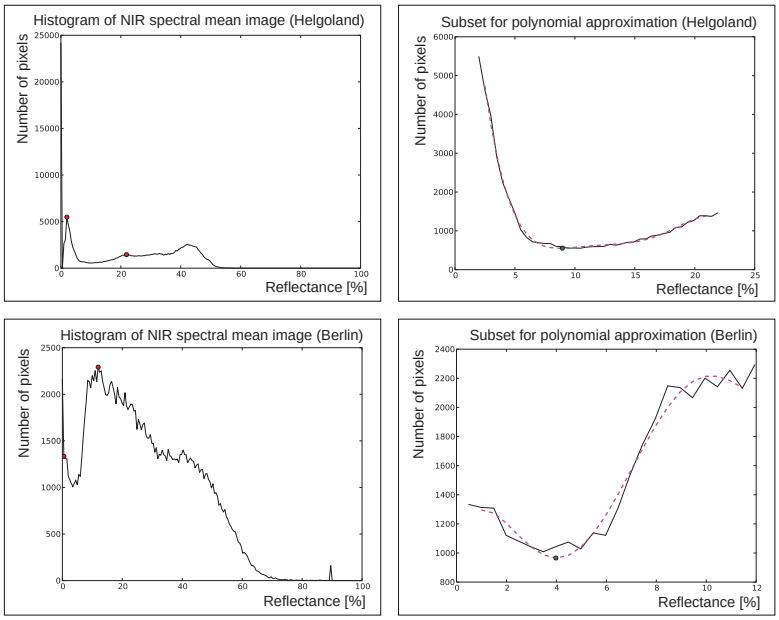

Fig. 5. Histograms (left: full, right: subset) of the NIR spectral mean images of two test sites (top: Helgoland, bottom: Berlin)

maximum) and a point near to the second local maximum (red dots in Fig. 5) the histogram between these two points is approximated by a polynomial of degree 5 (magenta dashed lines in Fig. 5). Then, the x value at the local minimum of the polynomial plus a safety margin of 2 is taken as the maximum reflectance threshold to be applied on the NIR spectral mean image. This results in a low albedo mask shown exemplarily for the test site Potsdam in Fig. 6. From this mask the water pixels have to be identified and other low albedo surfaces (mostly shadow) have to be removed.

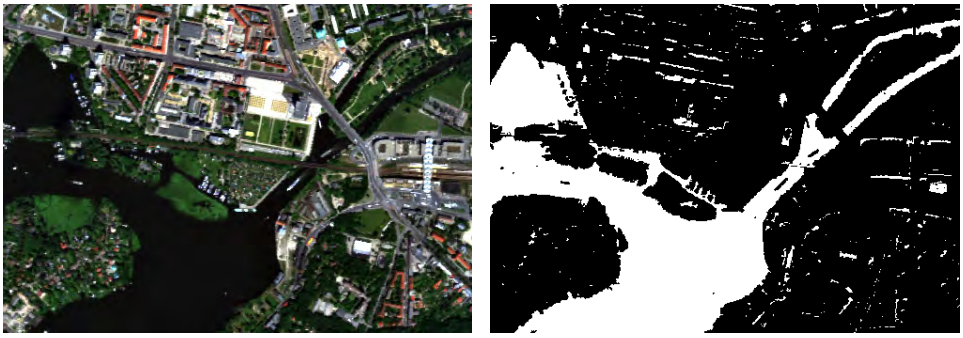

Fig. 6. Low albedo mask (right-hand) for the test site Potsdam

4.2 Differentiation between macrophytes in water and vegetation under shadow on land

Reflectance spectra of macrophytes (big emergent, submergent, or floating water plants) are characterized by spectral features of vegetation, such as the chlorophyll absorption features in the blue and red wavelength regions and the red edge in the NIR wavelength region. The light absorbing properties of water result in reflectance spectra exhibiting a comparably low albedo to those of shadowed vegetation on land (Fig. 7). Therefore, shadowed vegetation cannot be removed from the low albedo mask by simply thresholding an NDVI image.

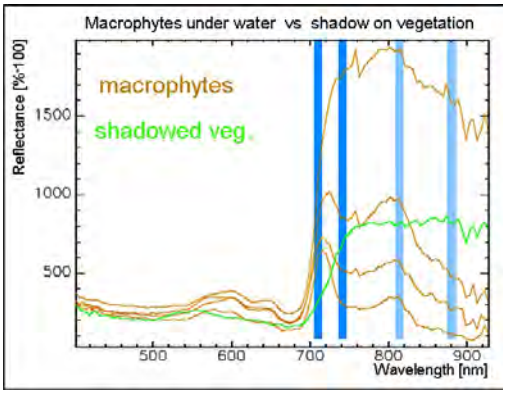

Fig. 7. Reflectance spectra of macrophytes in comparison with a reflectance spectrum of shadowed vegetation on land. The blue bars mark the wavelength of the two ratios used for distinguishing both surface types

However, a diagnostic spectral difference between both surfaces can be found in the NIR spectral region where the increasing water absorption causes the reflectance spectra of macrophytes to decrease between 710 – 740 nm as well as 815 – 880 nm. Therefore, pixels of shadowed vegetation can be removed from the low albedo mask using the condition:

$$VI^* > 1.0 \quad AND \quad (R_{740} - R_{710} / 740 - 710 < -0.001 \quad OR \quad R_{880} - R_{815} / 880 - 815 < -0.01) \quad (3)$$

where

VI^* = modified vegetation index = $\max(R_{710}, R_{720}) / R_{680}$
R_{740} = reflectance at wavelength 740 nm
Reflectance values must be scaled between 0 – 100

4.3 Removal of shadow pixels

Water and shadow reflectance spectra are on average both very dark. The reflectance level of both decreases with wavelength due to a decreasing proportion of diffuse irradiation (case of shadow) and due to the increasing light absorption (case of water). Additionally, both show a high spectral variability due to different types of shadowed surfaces (case of shadow) and due to varying water constituents and bottom reflection (case of water). However, despite this variation all water reflectance spectra have one thing in common: the pure water itself. Therefore, spectral features of pure water, especially absorption features, can be seen in every reflectance spectrum of water. However, the presence of these spectral features depends on the spectral superimposition of the water constituents and bottom coverage. Section 4.3.1 describes how these aspects can be considered in the development of a knowledge-based classifier for spectrally distinguishing water and shadow. Section 4.3.2 then continues with a spatial analysis.

4.3.1 Spectral analysis for water-shadow-separation based on spectral slopes

Fig. 8 shows the absorption spectrum of pure water (logarithmic scale) in comparison with selected surface reflectance spectra of different water bodies of the analyzed datasets. It can be seen that the increasing absorption within specific wavelength intervals (1st, 2nd, 4th and 5th light red bar) results in decreasing reflectance for most of the reflectance spectra. The 3rd light red bar represents a short wavelength interval of stagnating absorption where some water reflectance spectra temporarily rise due to increasing reflectance of water constituents or water bottom before decreasing again. However, these effects are not present within all wavelength intervals of all water reflectance spectra because they can be superimposed by the reflectance of the water constituents and water bottom. In order to find the slope combinations that occur for typical water bodies we analyzed 112.041 surface reflectance spectra from five datasets (two from Helgoland, two from Berlin, one from Potsdam). The selected datasets contain several types of water bodies (rivers, lakes, ponds, North Sea; transparent to productive and turbid waters). A first-degree polynomial was fitted to the spectra within each of the five wavelength intervals using the least squares method. If the algebraic sign of the slope within a wavelength interval met the expectation it was coded to 1 otherwise to 0. This resulted in a five-digit binary vector for each analyzed water reflectance spectrum representing the co-occurrence of slopes within the respective diagnostic wavelength intervals that met the expectation. The 25 possible binary vectors

were numbered from 0 to 31 whereas the 0 vector (none of the 5 slopes met the expectation) was excluded from further analysis. The numbered combinations are shown in Fig. 9 in comparison with the numbered combinations of 33.721 analyzed shadow spectra. It can be seen that many combinations are occupied either by water or by shadow spectra and thus provide a clear separation between water and shadow. These combinations are implemented in the developed approach so that applied to an image many pixels of the low albedo mask can either be identified as water or rejected as shadow. The other combinations marked by the orange arrows are ambiguous. Pixels that fall into these combinations need a consecutive spatial processing described in Section 4.3.2.

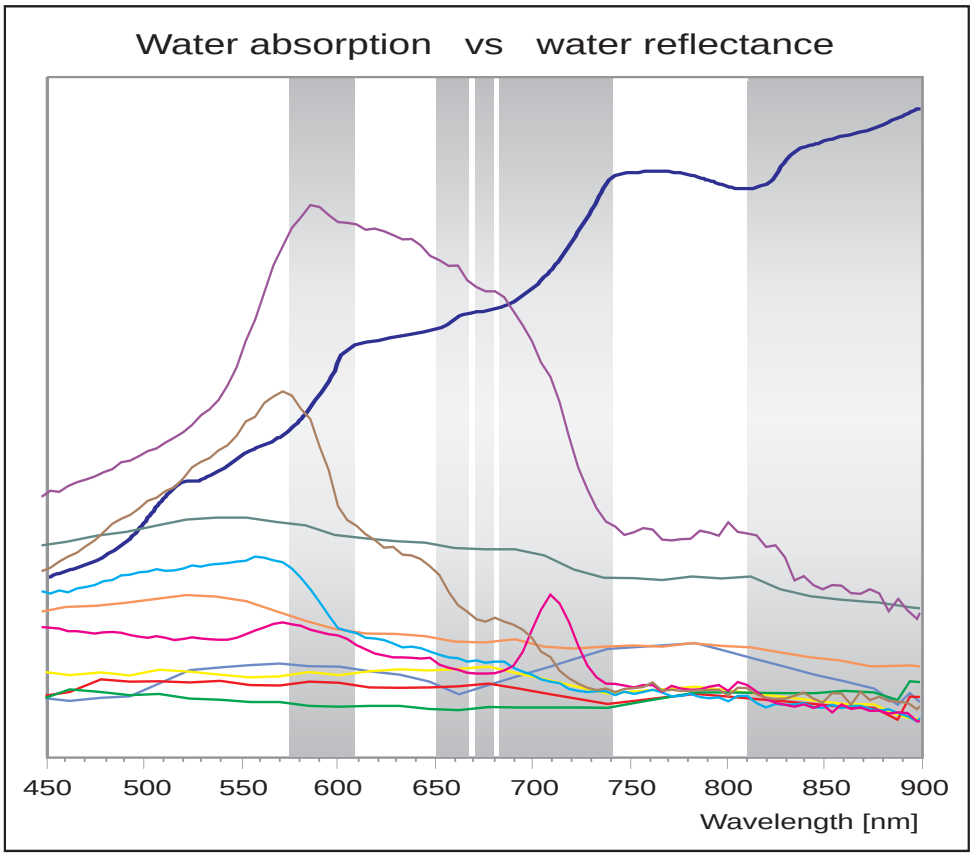

Fig. 8. Absorption of pure water (thick blue line, logarithmic scale, source: WASI (Gege, 2005)) in comparison to water surface reflectance spectra from different water bodies of the analyzed datasets. The increasing absorption within specific wavelength intervals (light red bars) results in decreasing reflectance for most of the reflectance spectra but is partly superimposed by the reflectance of the water constituents and water bottom

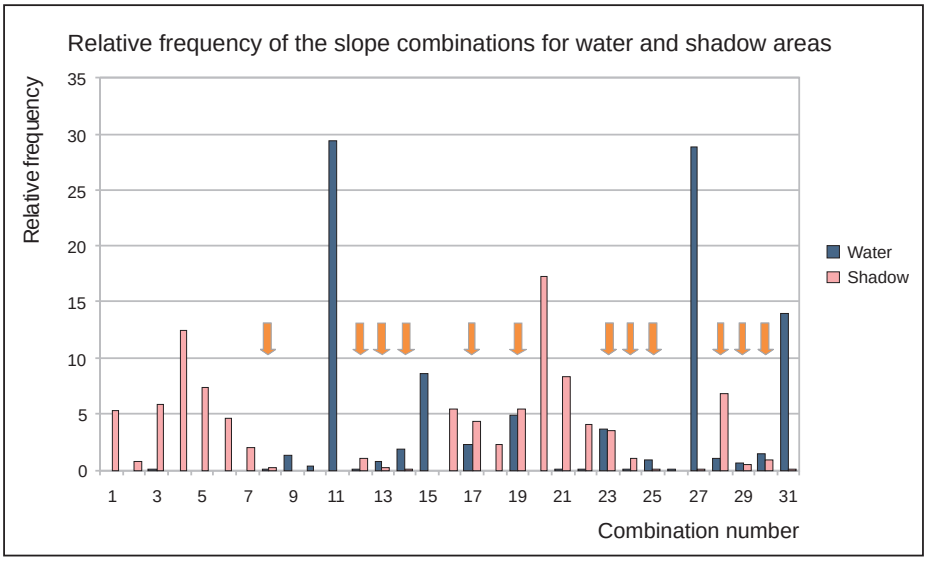

Fig. 9. Numbered slope combinations for water and shadow reflectance spectra. Due to the different amount of analyzed pixels of water and shadow (112.041 and 33.721) the *relative* frequency per land cover class is given. Combinations that are occupied by only one bar (or one very big and one very small bar) provide a clear separation between water and shadow. The combinations marked by the orange arrows are spectrally ambiguous

4.3.2 Spatial analysis for water-shadow-separation

Pixels of the low albedo mask that have not been identified as water or shadow based on the unambiguous spectral slope combinations are subjected to a consecutive spatial analysis. In this processing the idea is to decide according to the dominating spectral decision (see previous section) made within the neighbourhood of the ambiguous pixels (Fig. 10). The spectral decisions in the neighbourhood are counted using a 3x3 filter kernel resulting in a water score and a no-water score for each ambiguous pixel. If one of the two scores is more than three times higher than the other the ambiguous pixel is either identified as water or as no-water and is written into the respective image of confirmed water or no-water areas. If this is not the case the filter kernel iteratively grows up to a size of 33x33. Thereby, the identified water and no-water pixels are written into the respective image of identified water or no-water areas after each iteration so that they can be counted by the filter of the following iterations. When the filter kernel has reached a size of 33x33 and there are still ambiguous pixels left the decision threshold is reduced to two times higher than the other score and the filter kernel is reset to a size of 3x3. When the filter kernel reached a size of 33x33 for the second time it is again reset to a size of 3x3 and the decision is then simply related to the higher score. At this stage the filter starts growing again without a limit and until a decision was made for every ambiguous pixel. The graduation of the decision threshold has the advantage that pixels with an unambiguous neighbourhood are confirmed first and then accounted for in the following iterations. Finally, after all pixels have been identified either by spectral or spatial processing, the spectrally or spatially identified water pixels are combined into the final water mask. A last

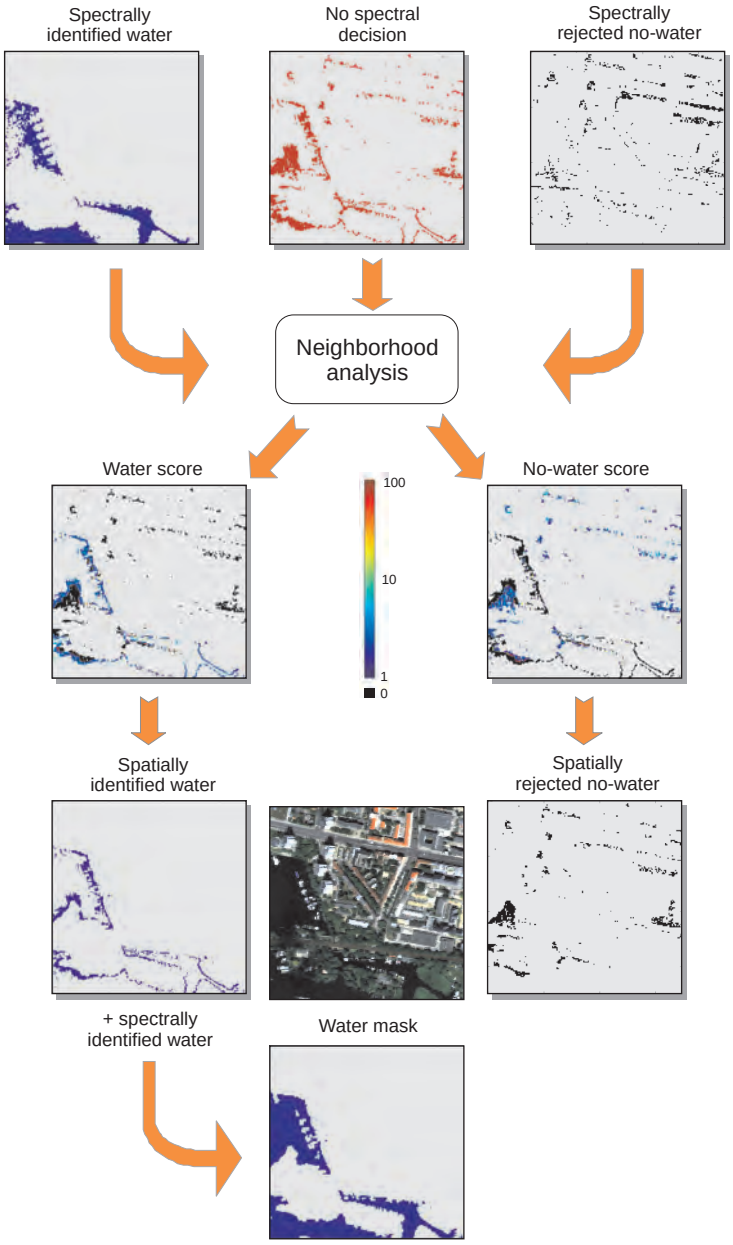

Fig. 10. Spatial processing illustrated by an exemplary subset of the Potsdam test site

aesthetic correction is done by filling up one pixel wholes within water areas which are considered as errors induced by noise. The filling of wholes can optionally be extended onto larger wholes (up to a certain size) which are likely to be boats (see Fig. 11).

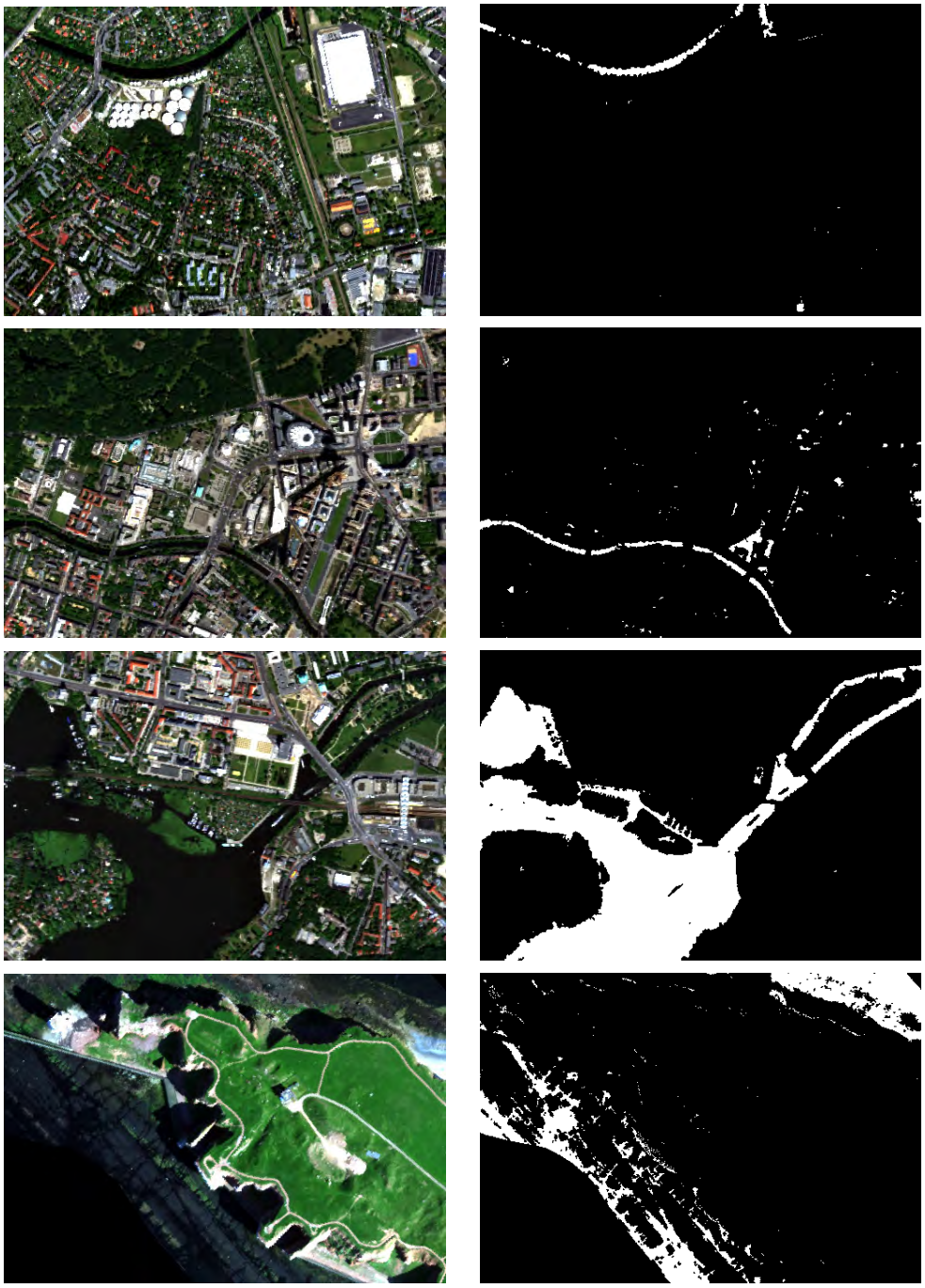

Fig. 11. (continued)

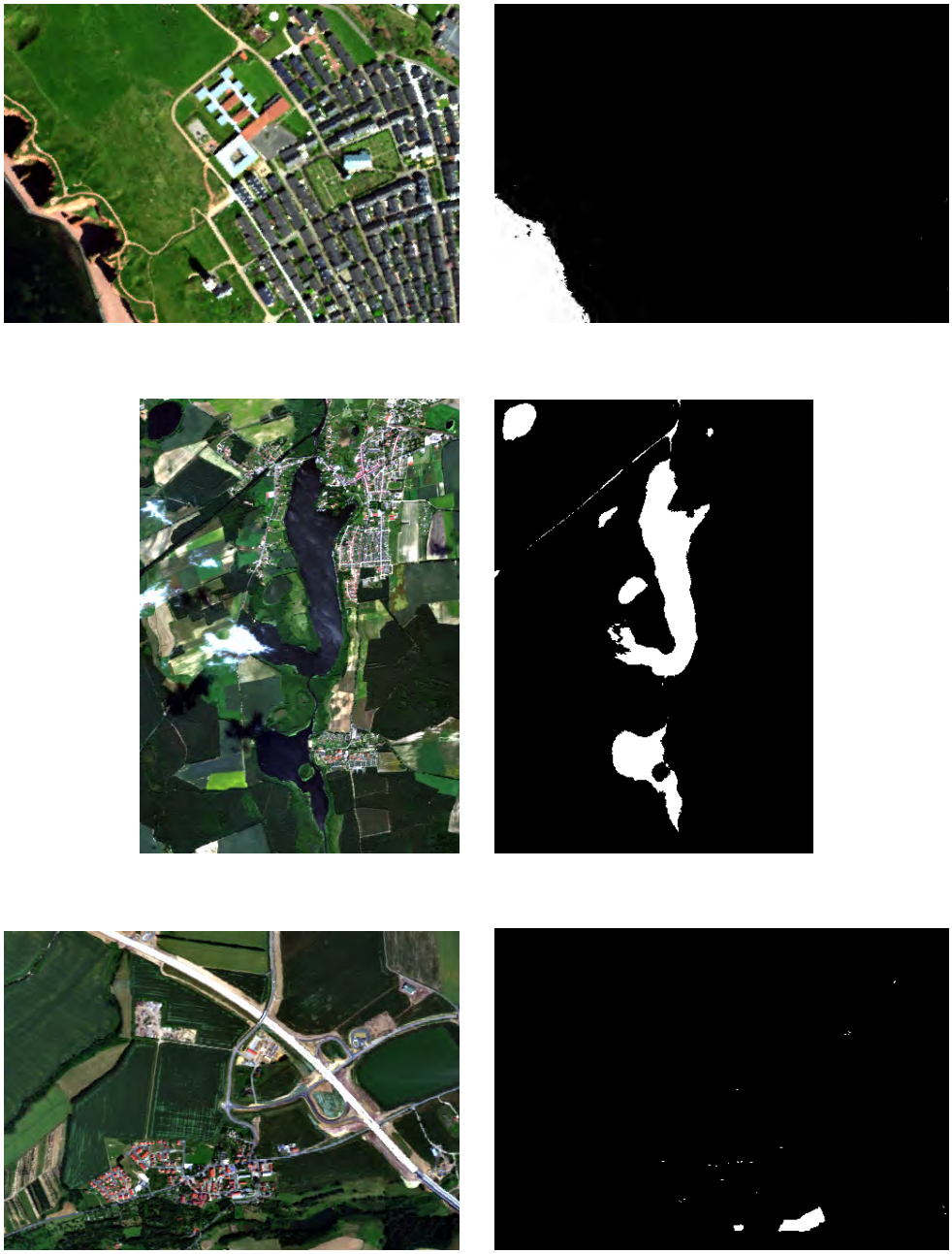

Fig. 11. (continued)

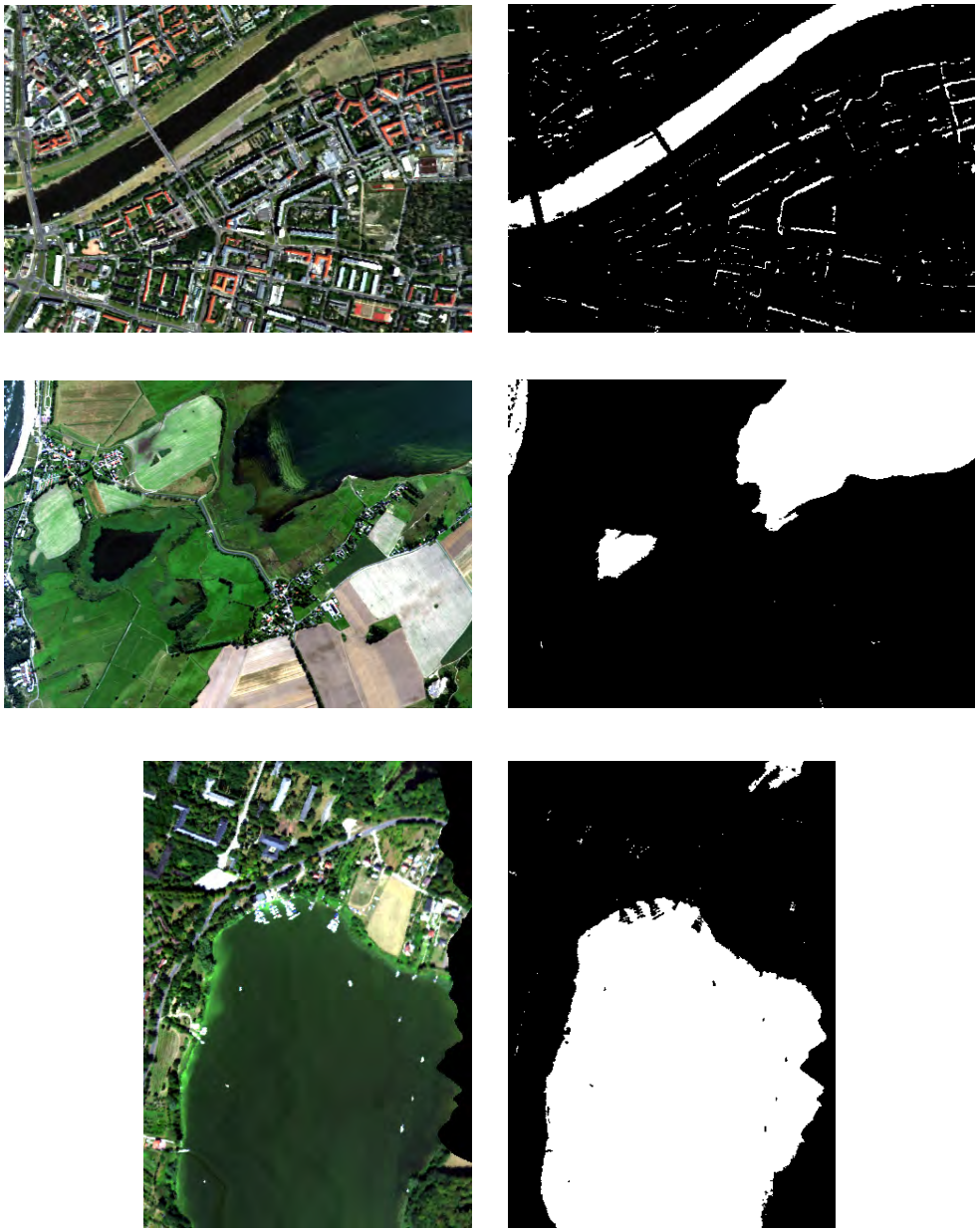

Fig. 11. Automatically detected water areas for the ten test sites Berlin_09:38, Berlin_10:12, Potsdam, Helgo_08:32, Helgo_09:26, Rheinsberg, Dresden_sub1, Dresden_sub2, Mönchsgut, Döberitzer (top to bottom; same order as in Tab. 3)

5. Results and discussion

In order to assess the accuracy of the developed approach water areas have been comprehensively digitized on-screen for selected validation sites of 175.000 pixels in size (350 by 500 or 500 by 350). The subsets have been chosen to contain as many challenging surface types as possible and to represent all different landscape types and sensors. Based on the digitized water reference areas no-water reference areas have been created by buffering the water reference areas with a two pixel buffer because of the mixed pixel problem and inverting the buffered areas. Using the reference areas of water and no-water several error metrics based on confusion matrices have been calculated. These are the probability of detection (POD), probability of false detection (POFD), false alarm ratio (FAR), overall accuracy (OA), average accuracy (AA) and kappa coefficient given in Tab. 3.

Test site	POD	POFD	FAR	OA	AA	Kappa
Berlin_09:38	79.5	0.1	9.6	99.8	89.7	0.845
Berlin_10:12	71.8	0.6	34.7	99.0	85.6	0.679
Potsdam	98.2	0.5	1.8	99.2	98.9	0.977
Helgo_08:32	99.8	2.3	25.3	97.8	98.8	0.843
Helgo_09:26	99.6	0.2	3.1	99.8	99.7	0.982
Rheinsberg	98.2	0.3	3.0	99.6	99.0	0.974
Dresden_sub1	98.7	0.0	7.9	100.0	99.3	0.953
Dresden_sub2	100.0	2.5	25.1	97.7	98.8	0.844
Mönchsgut	98.8	0.0	0.2	99.7	99.4	0.991
Döberitzer	100.0	1.8	1.9	99.1	99.1	0.981

Table 3. Results of the accuracy assessment. The first four test sites are subsets of datasets from which reflectance spectra have been analysed during the algorithm development. The last six test sites are subsets from independent validation datasets. The largest errors are highlighted in gray and discussed below.

The overall accuracy (a common error measure for classification results) amounts to 97% or above for all the test sites. However, to evaluate the detection accuracy of an underrepresented class the overall accuracy is not the best measure because it credits correct detections and correct not-detections equally and it is strongly influenced by the dominating class, i.e. the no-water class in this study. The overall measures average accuracy and especially kappa coefficient – although very high, too - reveal the remaining problems of the algorithm much better (highlighted in gray in Tab. 3). However, the most sensitive measures are the class-specific measures POD and FAR.

POFD, POD and FAR are typical measures for evaluating the accuracy of forecasting methods (Jolliffe & Stephenson, 2003) as well as two-class classification problems like detection tasks (one class of interest and one background class). The POFD of a class, also known as the false alarm rate, measures the fraction of false alarm pixels in relation to the

background class, i.e. the number of false alarm pixels divided by the total number of ground truth pixels of the background class (= omission error of the no-water class). The achieved POFDs for the test sites are very low (usually below 1 %) showing that water can be well distinguished from no-water surfaces. This is a big step forward compared to the NDWI and MNDWI which applied to high spatial resolution data result in many false positives for urban surface materials (see Fig. 3).

The POD of a class, also known as hit rate, measures the fraction of the detected pixels of the class of interest that were correctly identified, i.e. the number of correctly identified pixels divided by the total number of ground truth pixels of the class (= producer accuracy of the water class). The achieved PODs for most of the test sites are very high (> 98 %) showing that the developed algorithm usually detects almost all water pixels. False negatives occur only for small water bodies (small ponds within the park at the top left in Berlin_09:38, parts of the river in Berlin_10:12, and narrow rivers in Rheinsberg). Possible explanations are the adjacency effect (light from neighbouring pixels that is scattered into the instantaneous field of view by the atmosphere) and diffuse illumination of the water surface by surrounding trees. These two effects might be the reason for the spectral shape of the water spectra of small water bodies with surrounding trees that looks much more like a reflectance spectrum of vegetation than one of water (Fig. 12) and do not show the typical decreasing slopes that enabled the spectral identification of water as shown in section 4.3.1.

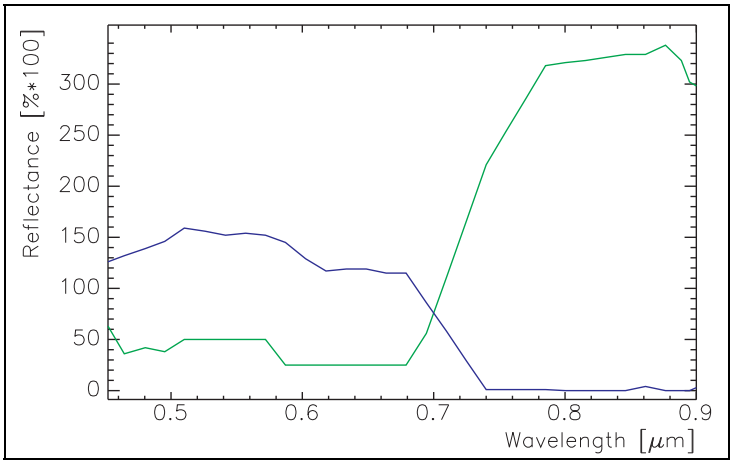

Fig. 12. A typical surface reflectance spectrum of water (blue) compared to a reflectance spectrum of a small water body with surrounding trees (green)

The false alarm ratio (FAR) gives the fraction of false alarm pixels in relation to the number of detected water pixels in the image, i.e. the number of false alarm pixels divided by the total number of classified water pixels (= commission error of water class). This error measure reveals clearly if to much water pixels have been falsely identified. This is the case for the test sites Berlin_10:12, Helgo_08:32, and Dresden_sub2 as well as in a weakened form for Berlin_09:38. In all of these test sites the confusion is related to shadow areas classified as water. For the test site Helgo_08:32 this can be explained by the intertidal zone which is wet even when the water is gone. Therefore, it is possible that there are some small water

influenced areas under the shadow which is a problem that has not yet been regarded in the water-shadow separation (section 4.3.1) and is still an open issue for the future.

Another open issue is the detection of white water pixels which are usually to bright to be included in the low albedo mask (section 4.1). This can be seen in the top left side of the test site Mönchsgut.

Overall, it can be seen from Tab. 3 that the accuracies of the independent datasets is not less than the accuracies of the datasets analyzed during the algorithm development. Thus, the algorithm seems to be robust and generalizes well to unknown datasets.

6. Conclusion

A new algorithm for the detection and delineation of surface water bodies based on high spatial resolution airborne VNIR imaging spectroscopy data has been developed. In contrast to existing methods the proposed approach does not require *a priori* knowledge nor user input, manual thresholding or fine-tuning of input parameters and is able to automatically detect and delineate surface water bodies with a very high accuracy. Thus, the developed algorithm is suitable for implementation in automated processing chains. The algorithm was tested on different sensor data (AISA Eagle and HyMap), works for different types of landscapes (tested: urban, rural and coastal) and is not influenced by different atmospheric correction methods (tested: ATCOR-4 (Richter, 2011), MIP (Heege & Fischer, 2004), ACUM-R (unpublished in-house development by K. Segl), the method of L. Guanter et al. (Guanter *et al.*, 2009), and empirical line correction). Future issues will be to improve the detection of small and narrow water bodies, the detection of white water and of water under shadow. Furthermore, the proposed method will be tested on hyperspectral VNIR satellite data.

7. Acknowledgement

This work was made possible by several flight campaigns carried out by the Deutsches Zentrum für Luft- und Raumfahrt (DLR) Oberpfaffenhofen, Germany. We further thank the people of the Geomatics Lab of the Humboldt University of Berlin for providing the HyMap data of Berlin. We also acknowledge financial support for AISA flight campaigns at Helgoland of the BIS Bremerhaven and the WFB Bremen in the framework of the projects 'Innohyp' and 'CoastEye'.

8. References

Alesheikh A.A., A. Ghorbanali & N. Nouri (2007). Coastline change detection using remote sensing. *International Journal of Environmental Science and Technology*, Vol. 4, No. 1, pp. 61-66

Buiteveld H., J.H.M. Hakvoort & M. Donze (1994). The optical properties of pure water. In: *Ocean Optics XII Proc. Soc. Photoopt. Inst. Eng.*, Vol. 2258, 174-183 pp.

Bukata R.P., J. Jerome, K.Y. Kondratyev & D.V. Pozdnyakov (1991). Optical properties and remote sensing of inland and coastal waters. *J. of Great Lakes Res.*, Vol. 17, pp. 461-469

Bukata R.P., J. Jerome, K.Y. Kondratyev & D.V. Pozdnyakov (1995). *Optical properties and remote sensing of inland and coastal waters*. CRC Press, Boca Raton, FL

Carleer A.P. & E. Wolff (2006). Urban land cover multi-level region-based classification of VHR data by selecting relevant features. *International Journal of Remote Sensing*, Vol. 27, No. 6, pp. 1035-1051

Cocks T., R. Jensen, A. Stewart, I. Wilson & T. Shields (1998). The HyMap airborne hyperspectral sensor: the system, calibration and performance. In: *Proc. of the 1st EARSeL Workshop on Imaging Spectroscopy*, Zürich.

Effler S.W. & M.T. Auer (1987). Optical heterogeneity in Green Bay *Water Resources Bulletin of the Geological Institutions of Uppsala*, Vol. 23, pp. 937-941

European Parliament and the Council of the European Union (2000). *European Water Framework Directive, Directive 2000/60/EC*. Vol. Official Journal L 327, European Union (Hrsg.), 0001-0073 p.

Frazier P.S. & K.J. Page (2000). Water body detection and delineation with Landsat TM data. *Photogrammetric Engineering and Remote Sensing*, Vol. 66, No. 12, pp. 1461-1467

Gege P. (2005). The Water Colour Simulator WASI - User manual for version 3. DLR-Interner Bericht, No. DLR-IB 564-1/2005, DLR, 83 p.

Guanter L., R. Richter & H. Kaufmann (2009). On the application of the MODTRAN4 atmospheric radiative transfer code to optical remote sensing. *International Journal of Remote Sensing*, Vol. 30, No. 6, pp. 1407-1424

Heege T. & J. Fischer (2004). Mapping of water constituents in Lake Constance using multispectral airborne scanner data and a physically based processing scheme. *Canadian Journal of Remote Sensing*, Vol. 30, No. 1, pp. 77-86

Ji L., L. Zhang & B. Wylie (2009). Analysis of Dynamic Thresholds for the Normalized Difference Water Index. *Photogrammetric Engineering and Remote Sensing*, Vol. 75, No. 11, pp. 1307-1317

Jolliffe I.T. & D.B. Stephenson (2003). *Forecast verification : a practitioner's guide in atmospheric science*. J. Wiley, Chichester, West Sussex, England, Hoboken, NJ

Lira J. (2006). Segmentation and morphology of open water bodies from multispectral images. *International Journal of Remote Sensing*, Vol. 27, No. 18, pp. 4015-4038

Manavalan P., P. Sathyanath & G.L. Rajegowda (1993). Digital image-analysis techniques to estimate waterspread for capacity evaluations of reservoirs. *Photogrammetric Engineering and Remote Sensing*, Vol. 59, No. 9, pp. 1389-1395

McFeeters S.K. (1996). The use of the normalized difference water index (NDWI) in the delineation of open water features. *International Journal of Remote Sensing*, Vol. 17, No. 7, pp. 1425-1432

Morel A. (1974). Optical properties of pure water and pure seawater, In: *Optical aspects of oceanography*, Jerlov N.G. & E. Steeman Nielsen (eds.), pp. 1-24, Academic, London

Müller J.L. & G.S. Fargion (2002). Ocean Optic Protocols for Satellite Ocean Colour Sensor Validation. Edited by NASA, Sensor Intercomparison and Merger for Biological and Interdisciplinary Ocean Studies (SIMBIOS) Project Technical Memoranda, 308 p.

Overton I.C. (2005). Modelling floodplain inundation on a regulated river: Integrating GIS, remote sensing and hydrological models. *River Research and Applications*, Vol. 21, No. 9, pp. 991-1001

Pope R.M. & E.S. Fry (1997). Absorption spectrum (380-700 nm) of pure water .2. Integrating cavity measurements. *Applied Optics*, Vol. 36, No. 33, pp. 8710-8723

Reigber S. *Erfassung limnologischer Parameter aus Gewässern des Norddeutschen Tieflandes mit hyperspektralen Fernerkundungsdaten. "Investigation of limnological parameters of inland waters in the North German Plain (Germany) using hyperspectral remote sensing data"*. PhD thesis, Computer Vision and Remote Sensing, Berlin University of Technology, Berlin.

Richter R. (2011). Atmospheric / topographic correction for airborne imagery. In: *ATCOR-4 user guide*, Software user guide, DLR - German Aerospace Center, Wessling, 167 p.

Roessner S., K. Segl, M. Bochow, U. Heiden, W. Heldens & H. Kaufmann (2011). Potential of hyperspectral remote sensing for analyzing the urban environment, In: *Urban Remote Sensing: Monitoring, Synthesis and Modeling in the Urban Environment,* Yang X. (ed.), pp. 49-62, Wiley, Oxford

Smith C.S. & K.J.S. Baker (1983). The analysis of ocean optical data. In: *7th SPIE, Ocean Optics*, Vol. 478, 119-126 pp.

Sogandares F.M. & E.S. Fry (1997). Absorption spectrum (340-640 nm) of pure water .1. Photothermal measurements. *Applied Optics*, Vol. 36, No. 33, pp. 8699-8709

Spectral Imaging Ltd. (2011). aisaEAGLE hyperspectral sensor.

Swain P.H. & S.M. Davis (1978). *Remote sensing : The quantitative approach*. McGraw-Hill International Book Co., New York

Work E.A. & D.S. Gilmer (1976). Utilization of satellite data for inventorying prairie ponds and lakes. *Photogrammetric Engineering and Remote Sensing*, Vol. 42, No. 5, pp. 685-694

Xiao G. & D. Tien (2010). An object-based classification approach for surface water detection. *Int. J. Intell. Syst. Technol. Appl.*, Vol. 9, No. 3/4, pp. 218-227

Xu H.Q. (2006). Modification of normalised difference water index (NDWI) to enhance open water features in remotely sensed imagery. *International Journal of Remote Sensing*, Vol. 27, No. 14, pp. 3025-3033